# Microenvironment influence on microtumour infiltration patterns: 3D-mathematical modelling supported by *in vitro* studies

Emmanuel Luján,[a,b] Daniela Soto,[c] María S. Rosito,[d] Alejandro Soba,[e] Liliana N. Guerra,[c,f] Juan C. Calvo,[c] Guillermo Marshall,[a] and Cecilia Suárez.*[a]

Mathematical modelling approaches became increasingly abundant in cancer research. Tumour infiltration extent and its spatial organization depend both on the tumour type and stage as well as on the bio-physicochemical characteristics of the microenvironment. This sets a complex scenario that often requires a multidisciplinary and individually-adjusted approach. The ultimate goal of this work is to present an experimental/numerical combined approach to develop a three-dimensional mathematical model able to reproduce the growth and infiltration pattern of a given avascular microtumour in response to the microenvironmental conditions. The model consists on a diffusion-convection-reaction equation that considers logistic proliferation, volumetric growth, a rim of proliferative cells at the tumour surface, and invasion with diffusive and convective components. Parameter values of the model were fitted to experimental results while radial velocity and diffusion coefficients were made spatially variable in a case-specific way through the introduction of a shape function and a diffusion-limited-aggregation (DLA)-derived fractal matrix, respectively, according to the infiltration pattern observed. The *in vitro* model consists of multicellular tumour spheroids (MTS) of an epithelial mammary tumour cell line (LM3) immersed in a collagen I gel matrix with standard culture medium ("naive" matrix) or conditioned medium from adipocytes or preadipocytes ("conditioned" matrix). It was experimentally determined that both adipocyte and preadipocyte conditioned media are able to change the *in vitro* infiltration pattern of MTS from a laminar to an individual and atomized one. Numerical simulations were able to adequately reproduce qualitatively and quantitatively both kinds of infiltration patterns, which was determined by area quantification, analysis of fractal dimensions and lacunarity, and a Bland-Altman analysis. These results suggest that the combined approach presented here could be established as a new framework with interesting potential applications both at the basic and clinical levels of the oncology area.

## Introduction

Cancer invasion is one of the hallmarks of cancer and a prerequisite for cancer metastasis. However, the invasion process is very complex and depends on multiple and correlated intrinsic and environmental factors. This makes it is difficult to be studied in a fully controlled way. The re-creation of the tumour microenvironment including a three-dimensional structure with tumour-stroma interactions, cell-cell adhesion and cellular signalling is essential for a deeper understanding of the tumour behaviour in general and the invasion process in particular[1]. In the context of a breast tumour, mammary fat may affect human breast cancer development. Recently it has been recognized the protumourigenic ability of matured adipocytes promoting proliferation and invasion of tumour cells *in vitro* and *in vivo*[2]. Conditioned medium from adipocytes significantly increases proliferation and survival of human mammary tumour cells *in vitro*[3]. Preadipocytes are also able to stimulate the growth of mammary tumour cells in culture[4].

Since *in vitro* models represent an over-simplification of the *in vivo* system, in these years it has been attempted to increase the level of complexity of *in vitro* assays to create models that could better mimic the behaviour of cells *in vivo*. This levels of complexity include, among others, the dimension of the system, moving

[a] *Instituto de Física del Plasma, CONICET-UBA, Buenos Aires, Argentina.*
[b] *Centro de Simulación Computacional para Aplicaciones Tecnológicas, CONICET, Buenos Aires, Argentina*
[c] *Departamento de Química Biológica, Facultad de Ciencias Exactas y Naturales, UBA, Buenos Aires, Argentina.*
[d] *Instituto de Astronomía y Física del Espacio, CONICET-UBA, Buenos Aires, Argentina*
[e] *Comisión Nacional de Energía Atómica, CONICET, Buenos Aires, Argentina*
[f] *Departamento de Ciencias Básicas, Universidad Nacional de Luján, Luján, Argentina*
* *Corresponding author. E-mail: csuarez@dc.uba.ar*

from two-dimensional to three-dimensional models[5]. Multicellular tumour spheroids (MTS) has been largely proposed as a predictive tool in cancer research, as they are physiologically useful *in vitro* models of a microtumour in the avascular stage[6,7]. When MTS are immersed in a three-dimensional biological matrix, the system is suited not only for therapeutic screening, but also for studying the growth and infiltration of the microtumour in response to the physico-chemical and biological characteristics of the microenvironment[8,9].

In mathematical oncology, numerical modelling emerged in the past decades with the intention of predicting the growth and infiltration of a tumour and its possible response to a given treatment[1,10]. So-called *in silico* trials aimed to predict patient-specific responses to various dose schedules or treatment combinations are becoming an invaluable tool to optimize patient care[11–13]. Agent-based tumour growth models are commonly used to describe the behaviour and interaction of individual cells in different environments[14,15]. Among continuous models, the use of ordinary differential equations (ODE) is an useful tool to simulate the evolution of total tumour cell number over time, though it lacks of spatial considerations[16]. Nevertheless in cancer, where the infiltration of tumour cells into normal tissue and the establishment of new distant metastasis are such crucial spatial aspects of the disease, the use of partial differential equations (PDE) are often more convenient. Relatively simple models based on reaction-diffusion equations of this kind that describe tumour proliferation and invasion into peripheral host tissues have proved to be of clinical relevance[17,18].

Computational simulation approaches focused on MTS can advance our understanding of cancer invasion and treatment[19–21]. Nevertheless, taking aside some specific cases[22–24], continuum models related to microtumour invasion have in general centered in the description of spherical tumour invasion areas. It is necessary at present to develop new strategies to better determine non-spherical tumour infiltration borders as well as to predict as much as possible tumour spread characteristics to optimize treatments such as surgery or radiotherapy. In a recent work, we introduced a two-dimensional mathematical model of microtumour growth and invasion in a collagen matrix, considering non-spherical invasion shapes[26].

Here we extended this work to a three-dimensional model able to reproduce, in a case-dependent manner, two very different infiltration patterns derived from different environmental conditions. In a first step, we tested experimentally the growth and infiltration pattern of MTS from mammary ephitelial origin with or without the presence of a conditioned medium from adipocytes or preadipocytes (fibroblasts) in the microenvironment. We then simulated the two types of invasion patterns observed *in vitro*. The approach presented here is applied in this case to a breast tumour type but it may be used with other tumour types, especially those where infiltration is a most important factor, like glioblastomas. This makes this experimental/numerical approach a potentially useful complementary clinical tool to help in tumour prognosis and treatment definition in a patient-specific way.

## Methods

### 1- *In vitro* model

#### Adipocyte differentiation and conditioned medium extraction

In this method, described in[27], 50.000 cells of the 3T3-L1 cell line (fibroblasts derived from murine embryonic tissue) were seeded in Dulbecco's modified Eagle medium (DMEM, Sigma-Aldrich) with 10% fetal bovine serum (FBS, Natocor). This line behaves as preadipocytes as cells can be differentiated to mature adipocytes in culture. For this, differentiating agents (Sigma-Aldrich) such as insulin 2 $\mu$M, 3-isobutil-1-metilxantine (IBMX) 0.5 $\mu$M and dexametasone 0.1 $\mu$M were added to the medium when cells are at 60-80% of confluence. Two and four days after, the medium was changed and insulin was renewed. At the sixth day, approximately 90-100% of the cells were differentiated, changing from fibroblast to amoeboid shapes and evidencing lipidic intracellular vesicles. Conditioned media were obtained from not-differentiated and differentiated (preadipocytes and adipocytes, respectively) cell cultures after three days in DMEM/FBS and stored at -20$^{\circ}C$ until their utilization.

#### MTS formation

Multicellular tumour spheroids of the LM3 cell line (mouse epithelial and metastatic mammary tumour cells[28]), were generated by the hanging drop method[29]. This technique has the advantage of producing homogeneous spheroids and consists on seeding drops of 20 $\mu l$ with 1.500 cells each, in the inner surface of a Petri dish cap. Once seeded, phosphate buffer solution (PBS) was placed in the base of the dish to maintain humidity and the cap returns to their natural position. Drops hang from the cap surface by superficial tension. After four days in culture at 37$^{\circ}C$ and 5% $CO_2$, one spheroid is formed at the bottom of each drop.

#### MTS seeding

Once formed, spheroids were recovered from the drops and immersed in a collagen I gel[30]. At this point two different experimental conditions were tested: spheroids immersed in collagen/DMEM ("naive" collagen) and spheroids immersed in collagen/conditioned medium from mature or immature adipocytes ("conditioned" collagen). For this, a rat tail collagen I (Gibco) solution 2 mg/ml in DMEM with 10% FBS (control group) or conditioned medium (treated groups) was prepared and placed on a six multi-well plate (0.5 ml/well). Ten spheroids were then placed on the surface of each well. After half an hour of incubation at 37$^{\circ}$ C, collagen solution becomes a gel and spheroids get immersed in it. Spheroids begin to invade the surrounding gel a day after seeding. Photographs were taken daily with an inverted optical microscope (Olympus) for seven days. Spheroid core and invasion areas were measured from photographs through the ImageJ software (http://imagej.nih.gov/ij). Experiments were repeated three independent times.

### 2- *In silico* model

The three-dimensional mathematical model represents an invading microtumour as a composition of two tumour cell populations with their own phenotype and behaviour: proliferative core cells

and invasive peripheral cells. This defines two domains under different mathematical resolution with a moving boundary determined by the core radius ($r_{core}$) between them: an inner domain corresponding to the growing core (core domain) and an outer domain corresponding to the infiltration area (infiltration domain). The model initiates from a single tumour cell and considers two stages: an initial benign stage where only core growth is considered and a later malignant stage where tumour infiltration is added to core growth. The benign stage is estimated in 10 days. During this time the spatial domain only consists on the core subdomain until the simulated microtumour reaches the radius corresponding to an specific experimental spheroid when seeded in collagen (invasion radius or $r_{inv}$). After that moment the spheroid begins invasion in the gel matrix and both spatial subdomains are present. This invasion has two components: an spherical (non-directional) and a radial or planar (directional) one.

**Core subdomain**

Core subdomain is an expanding area that describes the growth of the spheroid core. The inner boundary of this subdomain is defined by the minimum core radius ($r_{min}$). The outer moving boundary is defined by the core radius ($r_{core}$) calculated in spherical coordinates by:

$$r_{core}(t) = r_{min} + V_{core}\, t \tag{1}$$

being $V_{core}$ the core growth velocity and $t$ the time. Tumour cell concentration $C$ all inside this domain is equal to the tumour cell carrying capacity of the system $C_{max}$. The spheroid core, at t = 0, has an r = $r_{min}$ and a C = $C_{max}$. This corresponds to the placement of a single cell with a radius of 5 $\mu m$ in this subdomain. For both subdomains, $\phi$ is the azimuthal angle ($0 \leq \phi < 2\pi$) and $\theta$ the polar angle ($0 \leq \theta \leq \pi$).

**Infiltration subdomain**

In this domain, infiltrative tumour cell concentration follows a mass balance:

$$\frac{\partial C}{\partial t} = s - \nabla \cdot j \tag{2}$$

Where $s$ is the reaction term and $j$ is the mass flux. The reaction term is composed by two components:

$$s = P\, C \left(1 - \frac{C}{C_{max}}\right) + S\, \delta(r - r_{core}) \tag{3}$$

The first corresponds to the basal proliferation of the tumour cell population (logistic law), being $P$ the net proliferation rate. The second component represents a cell source ($S$) located at the spheroid surface ($r_{core}$) by the Dirac's delta function $\delta$, being $r$ the radius from the spheroid center. This corresponds to an external rim of specially proliferative cells present in this kind of microtumours.

On the other hand, the mass flux correspondent to tumour cell invasion is composed by a diffusive and a convective term:

$$j = -D\, \nabla C + V\, C \tag{4}$$

with $D$ being the diffusion coefficient and $V$ the invasion velocity. The diffusive term is based on the Fick's law and achieves the spherical non-directional component of the tumour invasion while the convective term represents the radial or planar (directional) component. Then the model can be expressed by a three-dimensional diffusion-convection-reaction equation[26]:

$$\frac{\partial C}{\partial t} = \nabla \cdot (D\, \nabla C) - \nabla \cdot (V\, C) + P\, C \left(1 - \frac{C}{C_{max}}\right) + S\, \delta(r - r_{core}) \tag{5}$$

In spherical coordinates:

$$\begin{aligned} \frac{\partial C}{\partial t} = {} & \frac{1}{r^2}\, \frac{\partial}{\partial r}\left(r^2\, D\, \frac{\partial C}{\partial r}\right) + \frac{1}{r^2\, sin(\theta)}\, \frac{\partial}{\partial \theta}\left(sin(\theta)\, D\, \frac{\partial C}{\partial \theta}\right) \\ & + \frac{1}{r^2\, sin^2(\theta)}\, \frac{\partial}{\partial \phi}\left(D \frac{\partial C}{\partial \phi}\right) - \frac{1}{r^2}\, \frac{\partial}{\partial r}\left(r^2\, C\, V_r\right) \\ & - \frac{1}{r\, sin(\theta)}\, \frac{\partial}{\partial \theta}\left(sin(\theta)\, C\, V_\theta\right) - \frac{1}{r\, sin(\theta)}\, \frac{\partial}{\partial \phi}\left(C\, V_\phi\right) \\ & + P\, C \left(1 - \frac{C}{C_{max}}\right) + S\, \delta(r - r_{core}) \end{aligned} \tag{6}$$

It is valuable to state that, in the case of simulations of individual infiltration, the convective term is null as planar invasion is achieved by the spatial variation of the diffusion coefficient $D$.

The inner boundary of the infiltration subdomain is $r_{core}(t)$ and the outer boundary is $r_{max}$. Due to the symmetry of the problem, in laminar simulations $\theta$ varies between 0 and $\pi/2$ instead of 0 and $\pi$. $V_r$, $V_\theta$ and $V_\phi$ are the components of the invasion velocity but, as the biology of the problem only conserves a radial component, $V_\phi$ and $V_\theta$ are null. The boundary condition at $r = r_{max}$ is $\frac{\partial C}{\partial r}(r_{max}, \phi, \theta) = 0$. Initial condition at t = 0 is $C(r, \phi, \theta) = 0$.

**Implementation**

Main parameter values are presented in table 1. Case-specific values were obtained from each individual experimental image. In order to obtain a more realistic description of the infiltration pattern, we made $V_r$ and $D$ spatially variable. In the case of laminar infiltrations, basal $V_r$ was made variable by the introduction of a shape function. In the case of individual infiltrations, basal $D$ was made variable by the introduction of a DLA-derived matrix. Otherwise, all infiltration areas would be spherical. By this way we make case-specific simulations in relation to core growth rate, infiltration pattern (laminar or individual), infiltration velocity and infiltration shape. The model was solved by finite differences with standard relaxation techniques and centered discretization with an order $O(h^2)$. It was implemented in C++ and parallelized through shared memory technology (OpenMP). Simulations were performed in an Intel(R) Core(TM) i7 processor, 2.2 GHzx8, 5.8 Gb, under Ubuntu Linux 16.04 LTS. In all cases, Paraview was used for image visualization (http://www.paraview.org/).

**Table 1** *In silico* model parameters

| Parameter | Value | Parameter | Value |
|---|---|---|---|
| $C_{max}$ | 0.0007 $cells/\mu m^3$ | $r_{min}$ | 5 $\mu m$ |
| $r_{inv}$ | case-specific | $r_{max}$ | 450 $\mu m$ |
| $V_{core}$ | case-specific | $P$ | 0.03 $cells/h$ |
| $S$ (laminar) | $4e^{-7}$ $cells/\mu m^3 h$ | $S$ (individual) | $9e^{-5}$ $cells/\mu m^3 h$ |
| $D$ (laminar) | 1.7 $\mu m^2 h^{-1}$ | $D$ (individual) | 70 $\mu m^2 h^{-1}$ |
| $V_r$ (laminar) | case-specific | | |

**Laminar infiltration pattern simulations**

In these simulations, a case-specific basal $V_r$ was made spatially variable along the azimuthal angle $\phi$ depending on a shape function. The shape function is extracted by image processing (through a C++ code written for this purpose) from each experimental image, and describe the invasion area contour of this tumour case, as it is explained in[26]. This function assigned weight along $\phi$ in the 360° domain based on the distance from the spheroid center to the external limit of the infiltration. Then the invasion contour curve is normalized and the correspondent invasion distance is calculated. Finally, the shape function was used to feed the main model to reproduce each experimental infiltration shape in a case-specific manner. The whole process is shown in figure 1.

**Individual infiltration pattern simulations**

This kind of simulation makes use of fractal structures. This was achieved by making basal $D$ spatially variable by the generation of a fractal 3D matrix derived from a modification of the DLA (diffusion limited aggregation) method[31,32]. Briefly, this method simulates the location of an original particle in the center of a three-dimensional box. Then other particles are released successively from the periphery of the box, move aleatory inside it and settle nearby another established particle. This finally achieves aggregated structures with fractal characteristics. Then the binary 3D fractal matrix determines the points where $D$ will have a zero or a non-zero value. 1000 different DLA matrices were generated by this method. This initial pool was used to select from it the best to fit with each experimental case of individual infiltration in base on shape similarities. This specific DLA-matrix was then used to feed the model and run a case-specific simulation.

Fractal characteristics (fractal dimension and lacunarity[33,34]) of all images were determined by the box-counting[35] and the glidling-box[36] method, respectively. Then, these characteristics were compared between experimental and simulated images by a Bland-Altman analysis[37,38] in order to determine the accuracy of the model. The analysis quantifies the level of similarity between two groups of study through the comparison of their main parametric statistics. This is achieved by constructing a linear regression curve with the substraction of correspondent statistics. This regression tends to be non-significant as groups are more similar between each other.

## Results and Discussion

Figure 2 shows two very different infiltration patterns observed experimentally. In both cases, a clear central spheroid area can be well differentiated from the peripheral invasion. MTS immersed in "naive" collagen present a collective and laminar invasion pattern, with polyhedric epithelial cells attached between each other (figure 2, left). On the contrary, the same spheroids immersed in collagen with adipocyte-conditioned medium ("conditioned" collagen) depict an individual and atomized invasion pattern, with rounded amoeboid cells separated from each other (figure 2, right). This was observed both with adipocyte- and preadipocyte-conditioned medium. It remains to be experimentally determined which specific soluble cell secretions are responsible for the observed effects.

Two main patterns of cancer cell invasion have been described so far: collective and individual. Among them, each specific pattern depends on the tumour cell type but also on the tumour microenvironment and stroma organization[39,40]. Human cancer pathology usually shows tumour cells invading collectively as strands, cords or clusters. *In vitro* studies display from single isolated cells with round or elongated phenotypes (amoeboid and fibroblast-like shapes, respectively) to loosely streams of cells or collective migration of cell strands or sheets. Experimental MTS cultures have revealed that collective epithelial cell invasion shows a leader-follower behaviour that is accompanied by an extensive extracellular matrix reorganization involving proteolysis and matrix alignment[41]. On the other hand, the passage from a laminar pattern to one with isolated cells suggests an epithelial-mesenchymal transition (EMT) of the infiltrating cells. This phenomenon is very common in the initial phases of cancer invasion and implies a phenotypic change marked by the loss of epithelial characteristics and the acquisition of invasive mesenchymal properties[42]. In vivo, both adipocytes and fibroblasts, main cellular components of the breast microenvironment, are known to secrete factors able to induce the EMT in epithelial mammary tumour cells (leptin and interleukin-6 for instance).

Figure 3 presents some examples of numerical simulations performed by the 3D model correspondent to laminar infiltration cases (MTS immersed in "naive" collagen), after five days of invasion. All parameter values were kept constant among the different simulations, except those relative to case-specificity, as $V_{core}$, $r_{inv}$, $V_r$ and the shape function. There is good qualitative agreement between each experimental case and its correspondent numerical simulation concerning both core growth and tumour infiltration. A whole simulation video about the first five days of infiltration is included as additional matherial ($Laminar - infiltration.avi$). Table 2 presents the quantification of the experimental and simulated image areas both for the MTS core and invasion zone, at the fifth day of invasion; the difference between them (calculated in relation to total invasion area); and the average difference. Averaged differences between experimental and simulated images are 12.57 % and 10.37 % for core and infiltrative areas, respectively. Then, simulations reproduce both qualitatively and quantitatively well the experimental cases.

Figure 4 shows some examples of numerical simulations performed by the 3D model correspondent to individual infiltration cases (MTS immersed in "conditioned" collagen), after five days of invasion. It can be observed a good qualitative correspondence between each experimental case and its correspondent fractal simulation. A whole simulation video about the

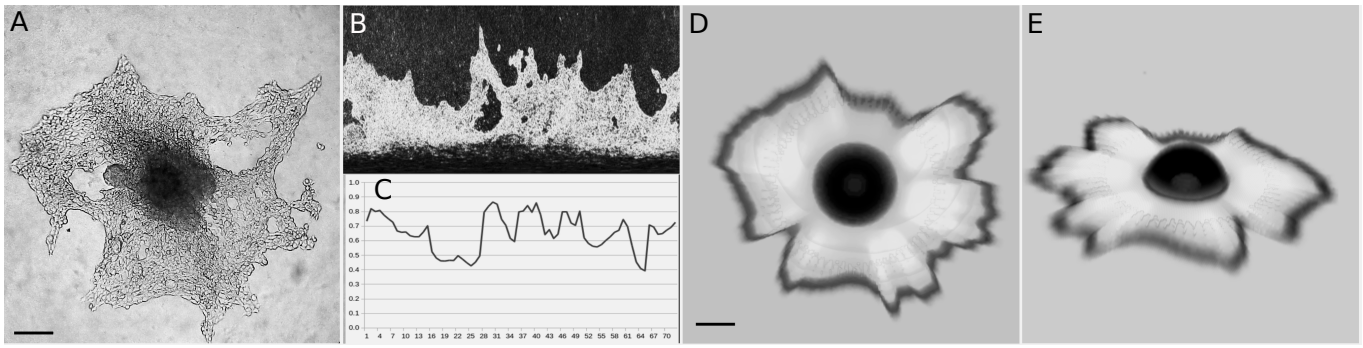


**Fig. 1** Image processing – A) Initial experimental image of an MTS invading a collagen matrix (100x). The central tumour core can be well differentiated from the peripheral invasion area. B) Image binarization and transformation from polar coordinates to Cartesian coordinates. C) Generation of the shape function (invasion distance vs. azimuthal angle $\phi$). D) and E) Different views of the final simulation that incorporates data from the shape function.

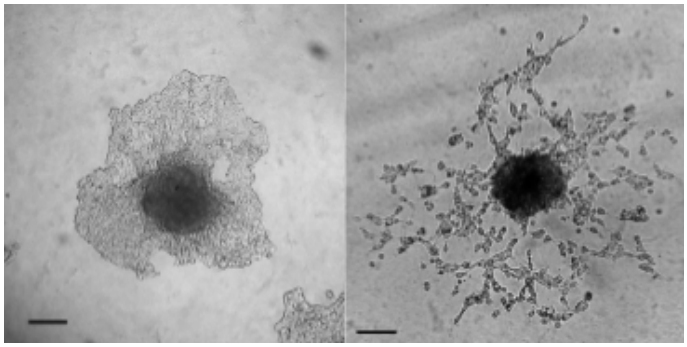

**Fig. 2** Experimental infiltration patterns – Micrographs of epithelial mammary MTS immersed in "naive" collagen (left) or in collagen with adipocyte-conditioned medium (right), both at the fifth day of invasion (scale bar: 100 $\mu m$).

**Table 2** Experimental and simulated core and invasion areas $(1x10^4 \mu m^2)$ with their correspondent differences and final average, for the MTS cases presented in figure 3.

| Case | Exp core | Sim core | Diff (%) | Exp inv | Sim inv | Diff (%) |
|---|---|---|---|---|---|---|
| 1 | 1.329 | 1.273 | 4.22 | 11.461 | 10.527 | 8.15 |
| 2 | 1.765 | 1.737 | 1.58 | 5.096 | 6.127 | 16.83 |
| 3 | 0.804 | 0.819 | 5.26 | 10.989 | 11.905 | 7.69 |
| 4 | 1.858 | 1.502 | 19.16 | 18.745 | 21.822 | 14.1 |
| 5 | 1.766 | 1.474 | 16.53 | 5.498 | 6.316 | 12.95 |
| 6 | 2.013 | 1.547 | 23.13 | 13.221 | 14.658 | 9.81 |
| 7 | 5.404 | 4.935 | 8.68 | 20.972 | 22.397 | 6.36 |
| 8 | 3.427 | 2.674 | 21.98 | 28.668 | 30.687 | 7.04 |
| | | Average | 12.57 | | Average | 10.37 |
| | | St. dev. | 8.05 | | St. dev. | 3.57 |

first five days of infiltration is included as additional matherial ($Individual-infiltration.avi$). In order to achieve a more quantitative analysis of these similarities, fractal properties (fractal dimension and lacunarity) of both types of images were compared. These two fractal properties are complementary, as fractal dimension quantifies how much of the total space is filled out by the object, while the lacunarity indicates how this space is filled out, giving an idea about symmetry-homogeneity and inner lacunar spaces. Laminar infiltration experimental images were also included in the comparison, as it is expected that DLA-derived simulations were more similar to the individual than to the laminar infiltration experimental cases.

Average fractal dimensions are significantly different among the three study groups (1.57 +/- 0.04, 1.49 +/- 0.03 and 1.68 +/- 0.07 for simulations of individual (atomized) infiltration, experimental individual infiltration and experimental laminar infiltration, respectively). Although local fractal dimensions (figure 5), determined by the box-count method, show a characteristic and distinctive pattern for each study group, the pattern presented by simulations of individual infiltration cases seems to be more similar to the individual than to the laminar infiltration experimental one, as expected.

Figure 6 depicts some characteristic lacunarity curves, derived by the gliding-box method, correspondent to the three types of images. Each subfigure presents the curve of a given individual infiltration case along with its correspondent simulation. The average lacunarity curve for laminar experimental cases was also included in all subfigures for comparison. It can be observed great qualitative similarity between lacunarity of individual infiltration cases and their corresponding simulations. On the other hand lacunarity curves from laminar infiltrations are very different.

In order to achieve some quantitative idea about the level of accuracy between individual infiltration experimental cases and their corresponding simulations, a Bland-Altman analysis about lacunarity curve correspondences was performed. A resultant non-significant linear regression intercept derived from this analysis is a sign of maximum similarity, while a non-significant regression slope indicates an independence between the similarity level and the magnitude of the statistic considered.

Figure 7 shows a comparison, by this method, of three lacunarity curve statistics (rank, standard deviation and average) derived from simulations of individual infiltration patterns with their correspondent experimental cases, on the one hand, and with experimental cases of laminar infiltration, on the other. It can be observed that, when comparing simulations with their correspondent experimental cases (first raw), both linear regression intercepts and slopes are non-significant in none of the three statistics considered (significance level at 5%). On the contrary, when comparing statistics from these simulations with the ones derived from laminar experimental cases (second raw), the observed differences, evidenced by the intercepts, are significant. Neverthe-

less, as linear regression slopes are not significant, these differences seem not to be related to the magnitude of the statistic considered.

These results mean that lacunarity curve statistics (and consequently lacunarity curves) derived from simulations of individual infiltration are significantly similar to the ones derived from their correspondent experimental cases and not to the laminar experimental ones. This indicates that the DLA-derived fractal approach is adequate to reproduce the individual infiltration pattern observed experimentally.

Although present personalized-medicine therapeutics tend to make increasing usage of *in vitro* three-dimensional models (in particular, tumour-derived spheroids) to test chemotherapy options in a patient-specific way[43–45], the *in vitro* model presented here does not intend to reproduce the *in vivo* hystological characteristics of the tumour invasion as it is well known that the invasion pattern of a given tumour may differ from in vivo to in vitro conditions. Nevertheless, even in *in vitro* conditions tumour cells do conserve much of their physiopathological characteristics and may give relevant information about tumour subtype and agressiveness. The approach proposed in this work aims to reveal these characteristics (specifically, spheroid growth rate, invasion growth rate and invasion pattern) that could feed a patient-specific predictive (or at least useful for prognosis estimation) mathematical model.

## Conclusions

Mathematical modelling approaches have become increasingly abundant in cancer research as they can refine treatment modalities at all phases of research and development, and in routine patient care. Infiltration issues are specially critical in many tumour types, as their correct determination is often essential to achieve a good tumour prognosis and/or surgery/radiotherapy optimization. Infiltration extent and its spatial organization depend both on the tumour type and stage as well as on the biophysicochemical characteristics of the stroma it encounters when spreading. This sets a complex scenario that often requires a multidisciplinary and individually-adjusted approach.

In a previous work we have proposed a combined method to study the invasion pattern of MTS immersed in a collagen matrix. Here, we proved that this approach is viable and useful applied in the context of an epithelial mammary microtumour that presents two very different infiltration patterns depending on the microenvironmental conditions. We showed experimentally that adipocyte and preadipocyte secretions are able to alter this pattern from a laminar and collective to an individual and atomized one.

We also presented a case-specific, three-dimensional numerical model based on a system of partial differential equations able to describe the microtumour growth as well as the two different infiltration patterns evidenced experimentally, in a more realistic way than previous models. This is achieved by making the radial velocity or the diffusion coefficient spatially variable. Numerical simulations were able to adequately reproduce these empirical data qualitatively and quantitatively for both infiltration patterns, as it was revealed by area quantification, fractal analysis (fractal dimensions and lacunarity), and a Bland-Altman analysis.

The *in vitro* model of multicellular tumour spheroids, combined with its correspondent mathematical modelling, has many experimental as well as clinical interesting potential applications in oncology. Results presented here suggest that our experimental/numerical approach could be established as a combined method to study possible invasion patterns that may result from different tumour types and microenvironmental conditions with potential usefulness at the moment of estimating clinical prognosis and designing tumour-treatment strategies in a context of a personalized medicine.

## Conflicts of interest

There are no conflicts of interest to declare.

## Acknowledgements

E. Luján and M. Rosito have fellowships from the Consejo Nacional de Investigaciones Científicas y Técnicas (CONICET). A. Soba, L.N. Guerra, J.C. Calvo, G. Marshall and C. Suárez are researchers at CONICET. This work was supported by grants from Universidad de Buenos Aires (UBACyT GC 20620130100027BA).

## References

1 A. Anderson, A. Weaver, P. Cummings and V. Quaranta, *Cell*, 2006, **127**, 905–915.

2 B. Wolfson, G. Eades and Q. Zhou, *World Journal of Biological Chemistry*, 2015, **6**, 39–47.

3 P. Iyengar, T. Combs, S. Shah, V. Gouon-Evans, P. J, C. Albanese, L. Flanagan, M. Tenniswood, C. Guha, M. Lisanti, R. Pestell and P. Scherer, *Oncogene*, 2003, **22**, 6408–6423.

4 H. Chamras, D. Bagga, E. Elstner, K. Setoodeh, H. Koeffler and D. Heber, *Nutrition and Cancer*, 1998, **32**, 59–63.

5 I. Manini, F. Caponnetto, A. Bartolini, T. Ius, L. Mariuzzi, C. Di Loreto, B. A and D. Cesselli, *International Journal of Molecular Sciences*, 2018, **19**, E147.

6 G. Benton, G. DeGray, H. Kleinman, J. George and I. Arnaoutova, *Plos One*, 2015, **10**, e0123312.

7 S. Nath and G. Devi, *Pharmacological Therapy*, 2016, **163**, 94–108.

8 A. Guzman, M. Ziperstein and L. Kaufman, *Biomaterials*, 2014, **35**, 6954–6963.

9 L. S, N. Arya, E. Kohler, S. Xiang, J. Christensen and S. V, *BMC Cancer*, 2016, **16**, 581.

10 L. Preziosi, *Cancer Modelling and Simulation*, Chapman & Hall/CRC, 2003.

11 P. Altrock, L. Liu and F. Michor, *Nature Reviews Cancer*, 2015, **15**, 730–745.

12 D. Barbolosi, J. Ciccolini, B. Lacarelle, F. Barlési and N. André, *Nature Reviews Clinical Oncology*, 2016, **13**, 242–254.

13 A. Karolak, D. Markov, L. McCawley and K. Rejniak, *J R Soc Interface*, 2018, **15**, Epub ahead of print.

14 Z. Wang, J. Butner, R. Kerketta, V. Cristini and T. Deisboeck, *Seminars in Cancer Biology*, 2015, **30**, 70–78.

15 J. Poleszczuk, P. Macklin and E. H, *Methods in Molecular Biology*, 2016, **1516**, 335–346.

16 H. Enderling and M. Chaplain, *Current Pharmaceutical Design*, 2014, **20**, 4934–4940.
17 C. Suárez, F. Maglietti, M. Colonna, K. Breitburd and G. Marshall, *PlosOne*, 2012, **7**, e39616.
18 P. Jackson, J. Juliano, A. Hawkins-Daarud, R. Rockne and K. Swanson, *Bull Math Biol*, 2015, **77**, 846–856.
19 D. Loessner, J. Little, G. Pettet and D. Hutmacher, *Journal of Cell Science*, 2013, **126**, 2761–2771.
20 D. Loessner, J. Flegg, H. Byrne, J. Clements and D. Hutmacher, *Integrative Biology*, 2013, **5**, 597–605.
21 L. Sander, *Cancer Research*, 2014, **74**, 4588–4596.
22 Y. Kim, S. Lawler, M. Nowicki, A. Chiocca and A. Friedman, *Journal of Theoretical Biology*, 2009, **260**, 359–371.
23 Y. Kam, K. Rejniak and A. Anderson, *Journal of Cell Physiology*, 2012, **227**, 431–438.
24 V. Andasari, R. Roper, M. Swat and M. Chaplain, *Plos One*, 2012, **7**, e33726.
25 A. Stein, T. Demuth, D. Mobley, M. Berens and L. Sander, *Biophysical Journal*, 2007, **92**, 356–365.
26 E. Luján, L. Guerra, A. Soba, N. Visacovsky, D. Gandía, J. Calvo and C. Suárez, *Integrative Biology*, 2016, **8**, 879–885.
27 L. Guerra, C. Suárez, D. Soto, A. Schiappacasse, D. Sapochnik, P. Sacca, G. Piwien-Pilipuk, B. Peral and J. Calvo, *Clinical and Translational Oncology*, 2015, **17**, 511–520.
28 A. Urtreger, V. Ladeda, L. Puricelli, A. Rivelli, M. Vidal, E. Sacerdote de Lustig and E. Bal de Kier Joffé, *International Journal of Oncology*, 1997, **11**, 489–496.
29 J. Kelm, N. Timmins, C. Brown, M. Fussenegger and L. Nielsen, *Biotechnological Bioengineering*, 2003, **83**, 173–180.
30 L. Kaufman, C. Brangwynne, K. Kasza, E. Filippidi, V. Gordon, T. Deisboeck and D. Weitz, *Biophysical Journal*, 2005, **89**, 635–650.
31 T. Witten and L. Sander, *Physical Review Letters*, 1981, **47**, 1400–1403.
32 L. Sander, *Contemporary Physics*, 2000, **41**, 203–218.
33 T. Smith, G. Lange and M. W, *Journal of Neuroscience Methods*, 1996, **69**, 123–136.
34 R. Plotnick, R. Gardner, W. Hargrove, K. Prestegaard and M. Perlmutter, *Physical Review E*, 1996, **53**, 5461–5468.
35 A. Kruger, *Computer Physics Communications*, 1996, **98**, 224–234.
36 C. Tolle and D. McJunkin, T Gorsich, *Physica D: Nonlinear Phenomena*, 2008, **237**, 306–315.
37 J. Bland and D. Altman, *Lancet*, 1986, **1**, 307–310.
38 J. Bland and D. Altman, *Ultrasound in Obstetrics & Gynecology*, 2003, **22**, 85–93.
39 N. Krakhmal, M. Zavyalova, E. Denisov, S. Vtorushin and V. Perelmuter, *Acta Naturae*, 2015, **7**, 17–28.
40 A. Clark and D. Vignjevic, *Current Opinions in Cellular Biology*, 2015, **36**, 13–22.
41 S. Carey, A. Starchenko, M. A and R.-K. C, *Clinical & Experimental Metastasis*, 2013, **30**, 615–630.
42 D. Micalizzi, D. Haber and S. Maheswaran, *Molecular Oncology*, 2017, **11**, 770–780.
43 F. Yang, S. Nam, C. Brown, R. Zhao, R. Starr, Y. Ma, J. Xie, D. Horne, L. Malkas, R. Jove and R. Hickey, *Plos One*, 2014, **9**, e94443.
44 T. Ishiguro, H. Ohata, A. Sato, K. Yamawaki, T. Enomoto and K. Okamoto, *Cancer Science*, 2017, **108**, 283–289.
45 S. Munthe, B. Halle, H. Boldt, H. Christiansen, S. Schmidt, V. Kaimal, J. Xu, S. Zabludoff, J. Mollenhauer, F. Poulsen and B. Kristensen, *Journal of Neurooncology*, 2017, **132**, 45–54.

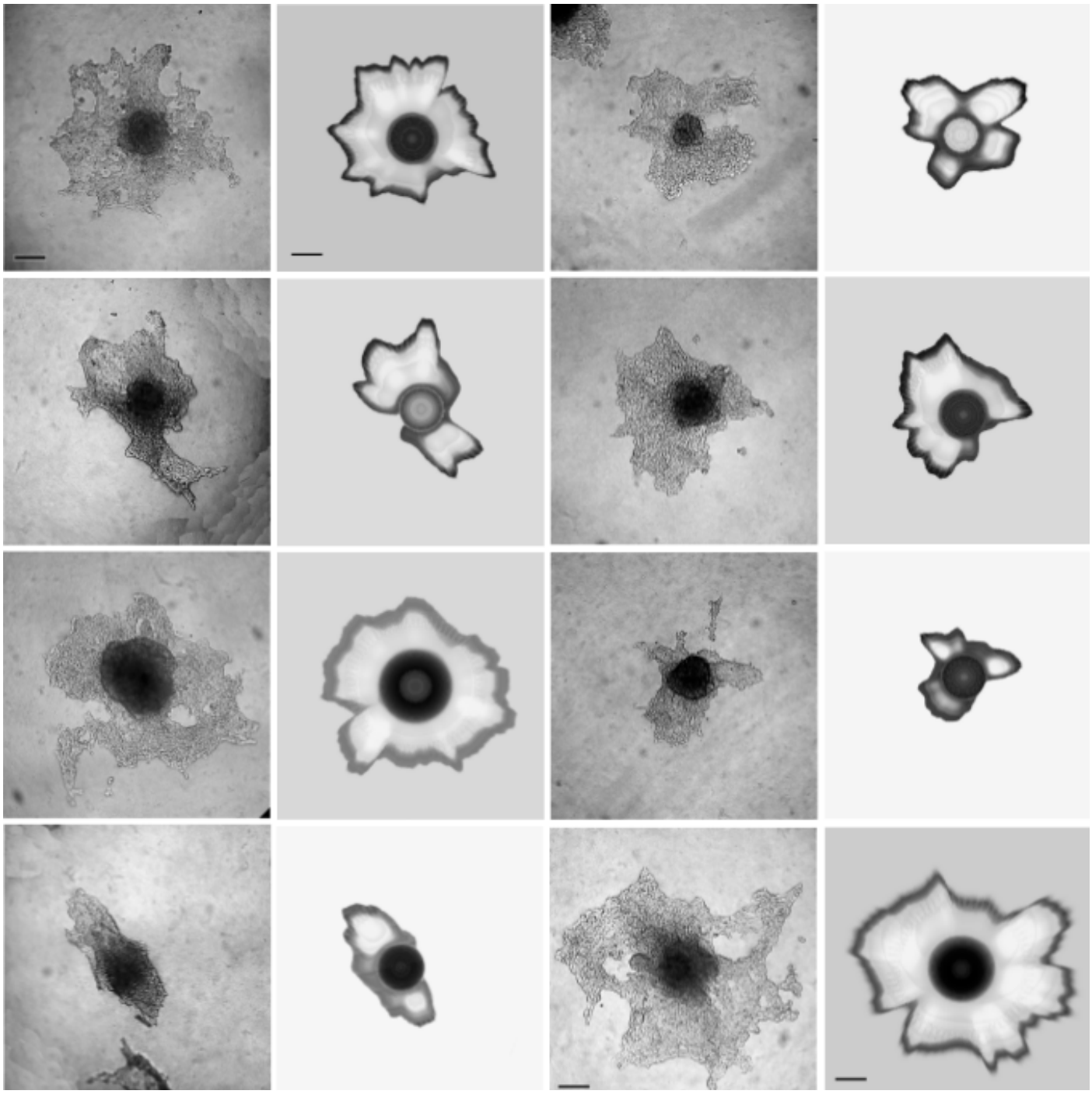

**Fig. 3** Laminar infiltration simulations – First and third columns: experimental images of epithelial mammary MTS at the 5th day of laminar infiltration into a "naive" collagen matrix (100x). Second and fourth columns: Numerical simulations corresponding to each experimental case, also at the 5th day of invasion (scale bar: 100 $\mu m$).

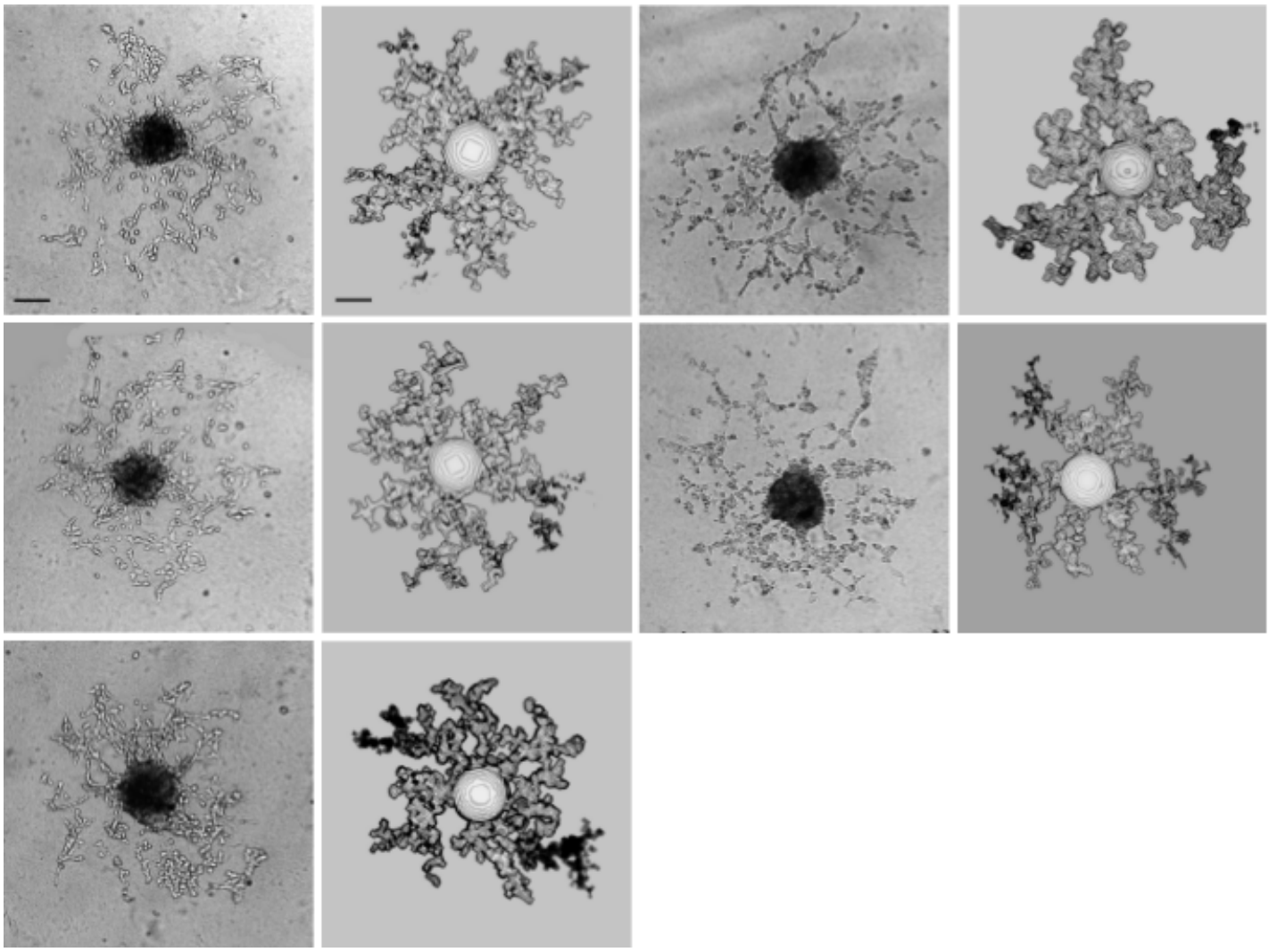

**Fig. 4** Individual infiltration simulations – First and third columns: experimental images of MTS at the 5th day of individual infiltration into a "conditioned" collagen matrix (100x). Second and fourth columns: Fractal simulations corresponding to each experimental case, also at the 5th day of invasion (scale bar: 100 $\mu m$).

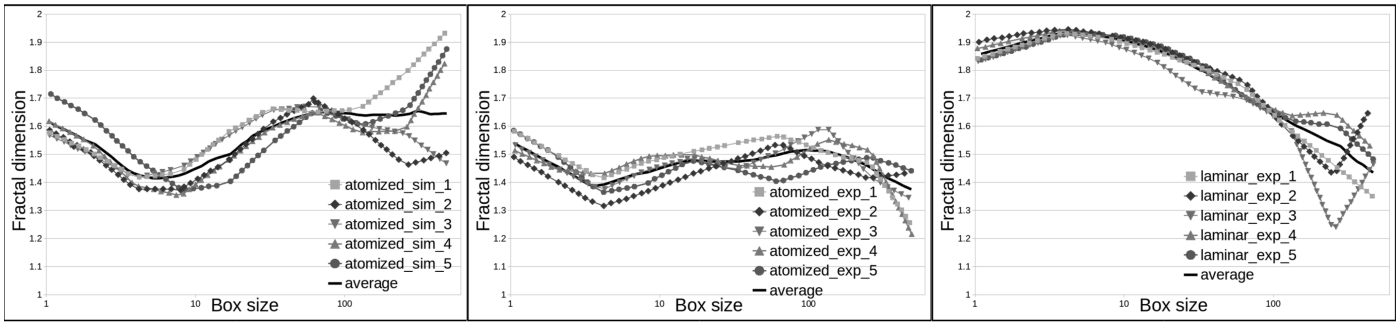


**Fig. 5** Local fractal dimensions – Fractal dimension vs. box size of five example cases for each type of image, with their correspondent average curve. Left: Curves derived from simulations of individual (atomized) infiltration cases. Center: Curves derived from individual infiltration cases. Right: Curves derived from laminar infiltration cases. All curves were obtained by the boxcount method.

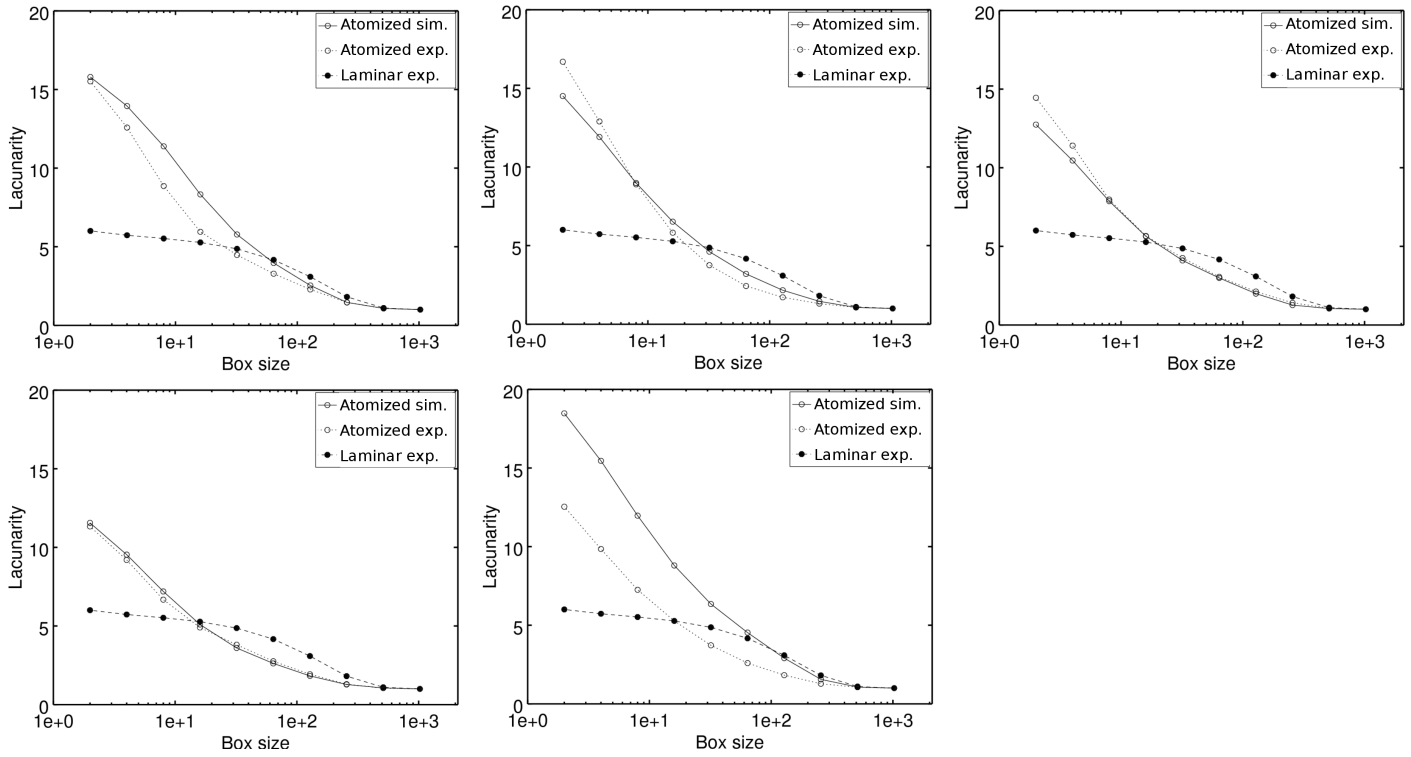


**Fig. 6** Lacunarity analysis – Lacunarity vs. box size for five examples of individual (atomized) infiltration. Each subfigure compares one experimental image (atomized exp.) with its correspondent simulation (atomized sim.). The average lacunarity curve resultant from laminar experimental cases was also included for comparison (laminar exp.). All curves were derived from the gliding-box method.

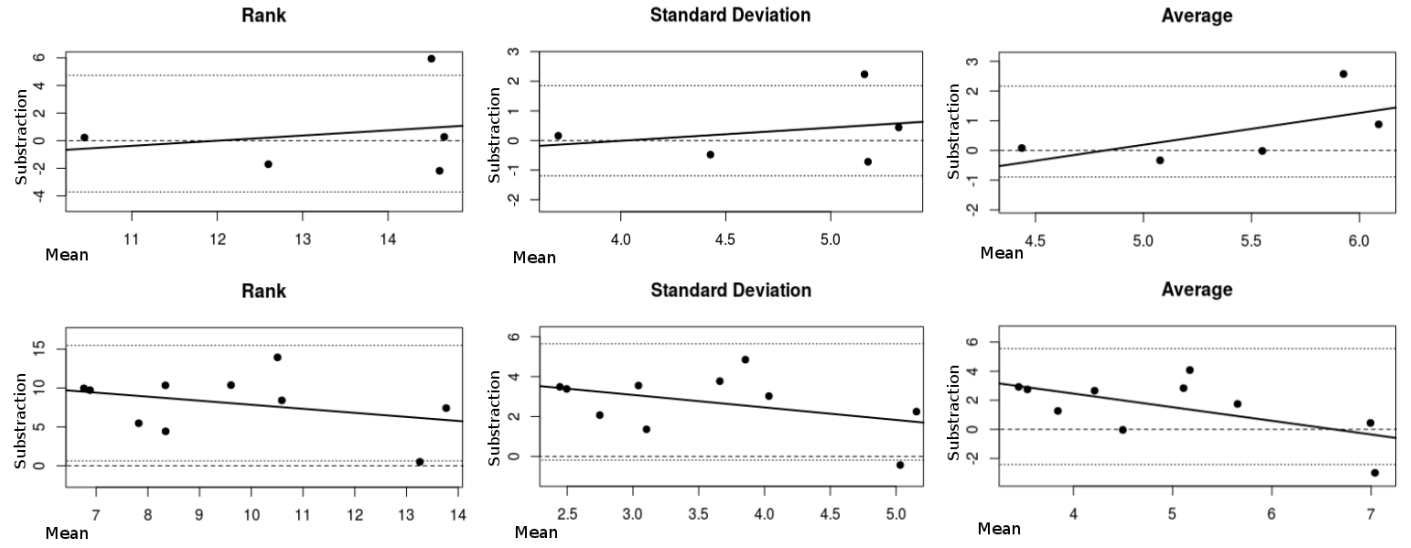


**Fig. 7** Bland-Altman analysis of lacunarity curves – Substraction of the compared statistic vs. its mean, for three statistics (rank, standard deviation and average) derived from the lacunarity curves considered. First raw: comparison between curves derived from simulations of individual infiltration cases and their correspondent experimental ones. Rank intercept: -4.49 (p=0.758), slope: 0.374 (p=0.73). Standard deviation intercept: -1.79 (p=0.72), slope: 0.445 (p=0.67). Average intercept: -5.17 (p=0.318), slope: 1.07 (p=0.269). Second raw: comparison between curves derived from the same simulations and those derived from laminar experimental ones. Rank intercept: 13.04 (p=0.0328), slope: -0.52 (p=0.34). Standard deviation intercept: 4.96 (p=0.0251), slope: -0.626 (p=0.238). Average intercept: 6.22 (p=0.0241), slope: -0.939 (p=0.0647).